Research Article

Investigation on Free Vibration of Rotating Cylindrical Shells with Variable Thickness

Liu Xiangdong,[1] Hou Xiaoli,[1] Bai Bin [ID],[2] and Zeng Maolin[1]

[1]*Hunan Sany Polytechnic College, Changsha 410000, China*
[2]*Hunan First Normal University, School of Intelligent Manufacturing, Changsha 410000, China*

Correspondence should be addressed to Bai Bin; baibin@126.com

In order to improve the performance and efficiency of the rotating cylindrical shell (RCS), one of the effective ways reduces the mass of the RCS. The scientific and effective method is to design the variable thickness of RCS (VTRCS) along the axial direction in response to this demand. Then, the vibration traveling wave characteristics of VTRCS are investigated by Chebyshev–Ritz method. The displacement field of the cylindrical shell is expanded in the form of the product of the Chebyshev polynomial and the boundary function. The kinetic and potential energies of the VTRCS are calculated based on the Sanders shell theory considering the effects of Coriolis forces and centrifugal forces. Also, the frequency equation of the VTRCS is obtained according to the Ritz method. The accuracy of the modeling method is verified by comparing the present results with literature that had done, and the convergence of the calculated results is studied. Finally, the free-vibration traveling wave characteristics of the VTRCS in different thickness variations are compared, and the parameters such as the rotational speed, thickness variation parameters, and aspect ratio on the free-vibration traveling wave characteristics of the VTRCS are discussed. The influence of thickness variation on the vibration characteristics is analyzed, which has significance for the lightweight design for VTRCS.

1. Introduction

The rotating cylindrical shell (RCS) is widely used in the industrial field, such as high-speed rotating centrifugal separator and rotor system of aeroengine. The RCS is increasingly demanding complex working condition in the engineering equipment; meanwhile, the wall thickness of the RCS shows the trend of more and more thin to meet the increasing of performance and efficiency, which lead to the structural vibration becoming more and more prominent. In addition, the RCS will have special traveling wave vibration phenomenon due to the influence of centrifugal force, Coriolis force, and the initial hoop tension compared with the static cylindrical shell; thus, it is of great significance to study the vibration characteristics of the RCS.

There are various solutions for the free vibration analysis of the RCS; for example, some scholars used Galerkin's method to analyze the free vibration characteristics of the RCS [1–5], and the differential quadrature method was also used to study the traveling wave properties of the free vibration for the RCS [6–11]. In addition, Ritz method was relatively simple in calculation process and could maintain high accuracy, so it was widely used in the research of vibration characteristics of RCS. For instance, Yan et al. [12] solved an accurate solution for the vibration-damping characteristics of a constrained stand-off-layer damping cylindrical shell and obtained the loss factor and the frequency based on the Hamilton principle. Song et al. [13] presented an improved Rayleigh–Ritz method to investigate the vibration and damping behavior of thin short cylindrical shell. Nguyen et al. [14] established sandwich structures and derived equations for the free vibration of rotating shells by the first-order, shear-deformation shell theory. Abbaspour and Hosseini [15] employed the Ritz method with Chebyshev polynomials to perform the free vibration analysis of the graphene platelets reinforced piezoelectric cylindrical microshells with various boundary conditions. Qin et al. [16–18] took Chebyshev polynomials as the admissible

functions, employed the Rayleigh–Ritz method to derive the motion equations for the rotating shell-plate combination, investigated the vibration of an RCS coupled with an annular plate based on the Sanders shell theory and Mindlin plate theory, and calculated the strain energy of the shell and plate. Then, they studied the free vibration of rotating functionally graded carbon nanotube reinforced composite cylindrical shells with arbitrary boundary conditions. Some scholars utilized Ritz method and Gram-Schmidt polynomials to form approximate functions and analyzed the free vibration of RCS [19]. Furthermore, some scholars studied the non-linear vibration of cylindrical shells of composite materials [20–24].

In addition, the abovementioned studies did not consider the influence of the thickness variation of the RCS. However, sometimes, the RCS needs to be designed with variable thickness in practice; that is, the thickness varies along the axial direction, and this can further reduce the weight. Therefore, some scholars analyzed the traveling wave vibration characteristics of rotating cylindrical shells with variable thickness (VTRCS). Quoc et al. [25] used Galerkin method to study the vibration characteristics of VTRCS under thermal environment, but only one thickness variation form was considered in this study.

Based on the above discussion, three different thickness variations are considered in this study, and Chebyshev–Ritz method is used to investigate the free vibration traveling wave behavior of VTRCS. Furthermore, the influences of parameters such as rotational speed, thickness variation parameters, and aspect ratio of cylindrical shells on the traveling wave behavior of free vibration for the VTRCS are discussed, which has significance for the lightweight design of rotating cylindrical shell structures.

High speed rotary drum has important application in centrifuge, which is abstracted to the rotating cylindrical shell (RCS) to reduce its mass and improve its performance and efficiency. The scientific and effective method is to design the variable thickness of RCS along the axial direction. In addition, the research can be applied to the aircraft engine disk or other mechanical structures and industrial fields, such as submarine, ship, drilling oil and gas field development, and factory workshop. Therefore, the research in this work has important application value in the fields of national defense and military.

2. Theoretical Modeling

Firstly, a theoretical model is established to study the traveling wave vibration characteristics of VTRCS. The cylindrical shell structure rotates around its central axis with a rotational speed Ω, its length is L, and its average radius is R. The (x, θ, z) is an orthogonal coordinate system established on the surface of the cylindrical shell, and u, v, and w are the dispositions of any point on the cylindrical shell along the three directions of x, θ, and z, respectively, as shown in Figure 1. It is assumed that the thickness $h(x)$ of the rotating cylindrical shell varies linearly along its axis, as

shown in Figure 2, which can be divided into three variation forms, denoted as $V1$, $V2$, and $V3$, respectively.

The coordinates of the upper and lower surfaces of the cylindrical shell in the Z direction of the coordinate axis will change under the three different thickness changes. The specific expressions are as follows.

The thickness change form of $V1$ is expressed as follows:

$$h_1(x) = -\frac{1}{2}\left(h_0\left(1 - k_h\frac{x}{L}\right)\right), \tag{1a}$$

$$h_2(x) = \frac{1}{2}\left(h_0\left(1 - k_h\frac{x}{L}\right)\right), \tag{1b}$$

where $h_1(x)$ and $h_2(x)$, respectively, represent the co-ordinates of the upper and lower surfaces of the cylindrical shell in the Z direction of the coordinate axis; h_0 represents the initial thickness of the cylindrical shell, that is, the thickness at $x = 0$; k_h represents the thickness variation parameter.

The thickness change form of $V2$ is expressed as follows:

$$h_1(x) = -\frac{h_0}{2}, h_2(x) = \frac{1}{2}\left(h_0\left(1 - k_h\frac{x}{L}\right)\right). \tag{2}$$

The thickness change form of $V3$ is expressed as follows:

$$h_1(x) = -\frac{1}{2}\left(h_0\left(1 - k_h\frac{x}{L}\right)\right),$$
$$h_2(x) = \frac{h_0}{2}. \tag{3}$$

2.1. Solution of Kinetic and Potential Energy. The Chebyshev–Ritz method is used to study the VTRCS in order to solve the natural frequency of the model. Firstly, the kinetic energy equation and potential energy equation of the cylindrical shell need to be given.

The velocity vector of any point on the VTRCS can be expressed as follows:

$$\mathbf{V} = \dot{\mathbf{r}} - \Omega \mathbf{i} \times (\mathbf{r} + R\mathbf{k}), \tag{4}$$

where k is the unit vectors along z direction and r represents the displacement vector of the VTRCS at any point on the coordinate system (x, θ, z), which can be described as follows:

$$\mathbf{r} = u\mathbf{i} + v\mathbf{j} + w\mathbf{k}, \tag{5}$$

where i, j, and k are, respectively, unit vectors along x, θ, and z directions.

The kinetic energy of the VTRCS can be calculated as follows:

$$T = \frac{1}{2}\int_0^{2\pi}\int_0^L\int_{h_1(x)}^{h_2(x)}\rho(\mathbf{V}\cdot\mathbf{V})Rdzdxd\theta, \tag{6}$$

Then, the kinetic energy equation of VTRCS is obtained by substituting equation (4) into equation (6), which is denoted as follows:
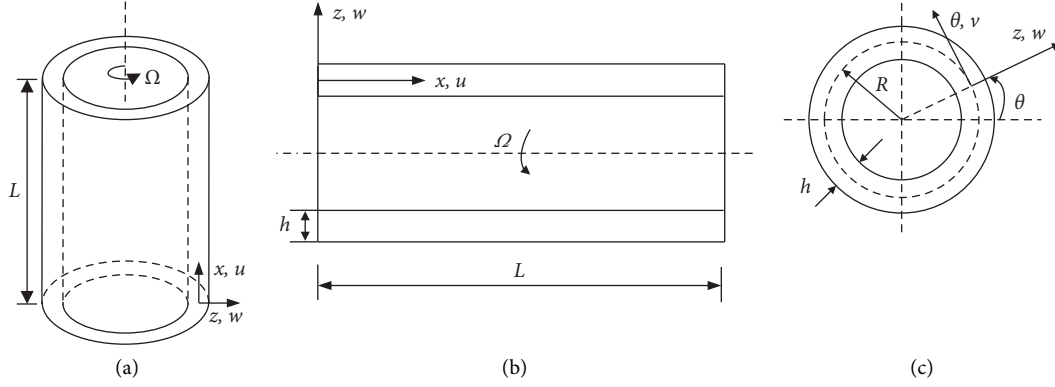
FIGURE 1: Schematic diagram of the RCS: (a) geometry configuration of the RCS and (b, c) coordinate system of the RCS.
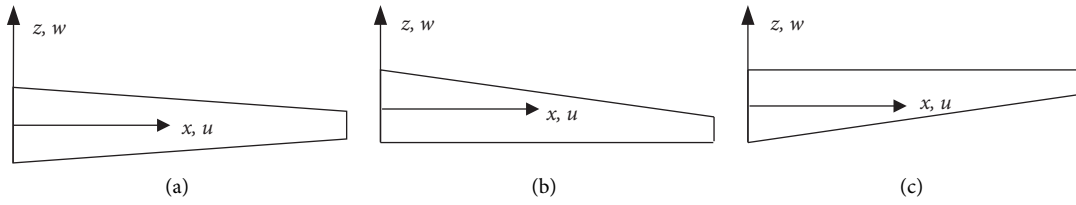
FIGURE 2: Three varying form of thickness for VTRCS. (a) $V1$. (b) $V2$. (c) $V3$.

$$T = \frac{\rho}{2} \int_0^{2\pi} \int_0^L \int_{h_1(x)}^{h_2(x)} \left(\dot{u}^2 + \left(\dot{v} + \Omega(w + R) \right)^2 + (\dot{w} - \Omega v)^2 \right) R dz dx d\theta.$$

(7)

According to Sanders shell theory, the strain at any point on the rotating cylindrical shell is written as follows:

$$\begin{cases} \varepsilon_{xx} = \varepsilon_{xx}^{(0)} + z \cdot \varepsilon_{xx}^{(1)}, \\ \varepsilon_{\theta\theta} = \varepsilon_{\theta\theta}^{(0)} + z \cdot \varepsilon_{\theta\theta}^{(1)}, \\ \gamma_{x\theta} = \gamma_{x\theta}^{(0)} + z \cdot \gamma_{x\theta}^{(1)}, \end{cases}$$

(8)

where $\varepsilon_{xx}^{(0)}$, $\varepsilon_{\theta\theta}^{(0)}$, and $\gamma_{x\theta}^{(0)}$ are the strain components of the middle surface and $\varepsilon_{xx}^{(1)}$, $\varepsilon_{\theta\theta}^{(1)}$, and $\gamma_{x\theta}^{(1)}$ are the curvature components of the middle surface. They can be expressed by the following formula [26]:

$$\begin{cases} \varepsilon_{xx}^{(0)} = \frac{\partial u}{\partial x}, \\ \varepsilon_{\theta\theta}^{(0)} = \frac{1}{R} \frac{\partial v}{\partial \theta} + \frac{w}{R}, \\ \gamma_{x\theta}^{(0)} = \frac{\partial v}{\partial x} + \frac{1}{R} \frac{\partial u}{\partial \theta}. \end{cases}$$

(9a)

$$\begin{cases} \varepsilon_{xx}^{(1)} = \frac{\partial^2 w}{\partial x^2}, \\ \varepsilon_{\theta\theta}^{(1)} = \frac{1}{R^2} \left(\frac{\partial v}{\partial \theta} - \frac{\partial^2 w}{\partial \theta^2} \right), \\ \gamma_{x\theta}^{(1)} = \frac{1}{R} \left(\frac{\partial v}{\partial x} - 2 \frac{\partial^2 w}{\partial x \partial \theta} \right). \end{cases}$$

(9b)

The stress-strain relationship of the VTRCS can be expressed as follows:

$$\left\{ \begin{array}{c} \sigma_x \\ \sigma_\theta \\ \tau_{x\theta} \end{array} \right\} = \begin{bmatrix} Q_{11} & Q_{12} & 0 \\ Q_{21} & Q_{22} & 0 \\ 0 & 0 & G \end{bmatrix} \left\{ \begin{array}{c} \varepsilon_{xx} \\ \varepsilon_{\theta\theta} \\ \gamma_{x\theta} \end{array} \right\}, \quad (10)$$

where $Q_{11} = Q_{22} = E/1 - \mu^2, Q_{12} = (\mu E)/(1 - \mu^2), G = E/2(1 + \mu)$.

The strain energy of the VTRCS caused by the deformation can be described as follows:

$$U_S = \int_0^{2\pi} \int_0^L \int_{h_1(x)}^{h_2(x)} \frac{1}{2} \cdot \left(\sigma_x \varepsilon_{xx}^{(0)} + \sigma_\theta \varepsilon_{\theta\theta}^{(0)} + \tau_{x\theta} \gamma_{x\theta}^{(0)} + z \left(\sigma_x \varepsilon_{xx}^{(1)} + \sigma_\theta \varepsilon_{\theta\theta}^{(1)} + \tau_{x\theta} \gamma_{x\theta}^{(1)} \right) \right) R dz dx d\theta. \quad (11)$$

The strain energy of the VTRCS caused by centrifugal force [27] is expressed as follows:

$$U_{CF} = \frac{\rho}{2} \cdot \int_0^{2\pi} \int_0^L \int_{h_1(x)}^{h_2(x)} R^2 \Omega^2 \left(\left(\frac{1}{R} \frac{\partial u}{\partial \theta} \right)^2 + \left(\frac{1}{R} \left(\frac{\partial v}{\partial \theta} + w \right) \right)^2 + \left(\frac{1}{R} \left(-\frac{\partial w}{\partial \theta} + v \right) \right)^2 \right) R dz dx d\theta. \quad (12)$$

Therefore, the total potential energy equation of the VTRCS with variable cross section can be expressed as follows:

$$U = U_S + U_{CF}. \quad (13)$$

The total potential energy solution of the VTRCS lays a foundation for studying its natural frequency and mode shape.

2.2. Solution of Natural Frequency and Mode Shape.

The natural frequency and mode shape of the VTRCS are solved in this section, and the solution process is given on the basis of the kinetic energy equation and potential energy equation obtained by the Chebyshev–Ritz method in the previous section.

Firstly, the displacement field of the VTRCS can be expressed as follows:

$$\left\{ \begin{array}{l} u = U(x) \cos(n\theta + wt), \\ v = V(x) \sin(n\theta + wt), \\ w = W(x) \cos(n\theta + wt), \end{array} \right. \quad (14)$$

where w is the natural frequency and n is the toroidal wave number of the traveling wave modal. $U(x)$, $V(x)$, and $W(x)$ are modal functions, which are approximately expanded by the product of Chebyshev polynomials and their corresponding boundary functions, and the specific formula is expressed as follows:

$$\left\{ \begin{array}{l} U(\xi) = \sum_i^{nmax} a_i f_u(\xi) P_i(\xi), \\ V(\xi) = \sum_j^{nmax} b_j f_v(\xi) P_j(\xi), \\ W(\xi) = \sum_k^{nmax} c_k f_w(\xi) P_k(\xi). \end{array} \right. \quad (15)$$

where a_i, b_j, and c_k are unknown coefficients and $P_i(\xi)$, $P_j(\xi)$, and $P_k(\xi)$ are the first kind Chebyshev expressions, which can be expressed in trigonometric terms as follows:

$$P_l(\xi) = \cos[(l - 1)\arccos(\xi)] \quad (l = i, j, k). \quad (16)$$

Chebyshev polynomials can achieve fast convergence speed and maintain high accuracy at a lower computational cost, but they are defined on the interval [−1, 1] and have orthogonality only on this interval, so coordinate transformation is needed, that is, $\xi = 2x/L - 1$. $f_u(\xi)$, $f_v(\xi)$, and $f_w(\xi)$ represent boundary functions along the ξ direction, which need to satisfy the corresponding geometric boundary conditions of the VTRCS, and the specific expressions are shown in Table 1.

Secondly, the displacement field equation (14) of the VTRCS is substituted into the kinetic energy equation (7), which can be further expressed as follows:

$$T = \frac{L\pi R I_0}{4} \int_{-1}^{1} \left(w^2 U(xi)^2 + w^2 V(xi)^2 + 4w\Omega V(xi)W(xi) + \right.$$

$$\left. 2\Omega^2 R^2 + w^2 W(xi)^2 + \Omega^2 \left(V(xi)^2 + W(xi)^2 \right) \right) d\xi. \quad (17)$$

TABLE 1: The boundary function for different boundary conditions.

	$f_u(\xi)$	$f_v(\xi)$	$f_w(\xi)$
F-S	1	$1 - \xi$	$1 - \xi$
S-F	1	$1 + \xi$	$1 + \xi$
S-S	1	$1 - \xi^2$	$1 - \xi^2$
F-C	$1 - \xi$	$1 - \xi$	$1 - \xi$
C-F	$1 + \xi$	$1 + \xi$	$1 + \xi$
C-C	$1 - \xi^2$	$1 - \xi^2$	$1 - \xi^2$

Similarly, equation (14) is substituted into equation (13), and the potential energy equation of the VTRCS can be expressed as follows:

$$
\begin{aligned}
U = \frac{\pi L}{4R^3} \int_{-1}^{1} & \left(\frac{16R^4 D_{11}}{L^4} \left(\frac{\partial^2 W(\xi)}{\partial \xi^2} \right)^2 - \frac{8R^2 n D_{12}}{L^2} (V(\xi) + nW(\xi)) \frac{\partial^2 W(\xi)}{\partial \xi^2} + , \right. \\
& \frac{4R^2}{L^2} \left(A_{66}R^2 + D_{66} \right) \left(\frac{\partial V(\xi)}{\partial \xi} \right)^2 - \frac{4R^2 n}{L} \left(RA_{66}U(\xi) - \frac{4D_{66}}{L} \frac{\partial W(\xi)}{\partial \xi} \right) \frac{\partial V(\xi)}{\partial \xi} + , \\
& \frac{4R^4 A_{11}}{L^2} \left(\frac{\partial U(\xi)}{\partial \xi} \right)^2 + \frac{4R^3 A_{12}}{L} (V(\xi)n + W(\xi)) \frac{\partial U(\xi)}{\partial \xi} + \frac{16R^2 D_{66} n^2}{L^2} \left(\frac{\partial W(\xi)}{\partial \xi} \right)^2 + , \\
& n^2 \left(A_{11}R^2 + D_{11} \right) V(\xi)^2 + 2n \left(A_{11}R^2 + D_{11}n^2 \right) V(\xi)W(\xi) + \left(D_{11}n^4 + A_{11}R^2 \right) W(\xi)^2 + , \\
& \left. R^2 U(\xi)^2 n^2 A_{66} + \frac{\Omega^2 RL\pi I_0}{4} \left((n^2 + 1) \left(V(\xi)^2 + W(\xi)^2 \right) + 4nV(\xi)W(\xi) + n^2 U(\xi)^2 \right) d\xi, \right.
\end{aligned}
\tag{18}
$$

where A_{11}, A_{12}, and A_{66} represent the tensile stiffness and D_{11}, D_{12}, and D_{66} represent the bending stiffness. The specific expressions are denoted as follows:

$$
\begin{aligned}
A_{11} &= \int_{h_1(x)}^{h_2(x)} Q_{11} dz = \int_{h_1(x)}^{h_2(x)} Q_{22} dz \\
A_{12} &= \int_{h_1(x)}^{h_2(x)} Q_{12} dz = \int_{h_1(x)}^{h_2(x)} Q_{21} dz \\
A_{66} &= \int_{h_1(x)}^{h_2(x)} G dz, \\
D_{11} &= \int_{h_1(x)}^{h_2(x)} Q_{11} z^2 dz = \int_{h_1(x)}^{h_2(x)} Q_{22} z^2 dz \\
D_{12} &= \int_{h_1(x)}^{h_2(x)} Q_{12} z^2 dz = \int_{h_1(x)}^{h_2(x)} Q_{21} z^2 dz \\
D_{66} &= \int_{h_1(x)}^{h_2(x)} G z^2 dz.
\end{aligned}
\tag{19}
$$

Then, according to equations (17) and (18), the energy expression of the VTRCS can be obtained as follows:

$$
\Pi = U - T.
\tag{20}
$$

The most likely approximate value is determined by minimizing the energy expression with respect to the unknown coefficient according to Rayleigh's principle, so the derivative of the energy expression with respect to the unknown coefficient is performed as follows:

$$
\frac{\partial \Pi}{\partial a_i} = 0, \frac{\partial \Pi}{\partial b_j} = 0, \frac{\partial \Pi}{\partial c_k} = 0 \ (i, j, k = 1, 2, ..., n\max).
\tag{21}
$$

Then, equation (21) can be further transformed into an eigenvalue matrix, which is written as follows:

$$
\left(\mathbf{K} - w^2 \mathbf{M1} - w\mathbf{M2} \right) \mathbf{P} = 0,
\tag{22}
$$

where K is the stiffness matrix, $M1$ and $M2$ are the mass matrices, w represents the natural frequency, and P is the eigenvector composed of unknown coefficients, namely, the mode shape of the VTRCS, which is expressed as follows:

$$
\mathbf{P} = \left[a_1, ..., a_i, b_1, ..., b_j, c_1, ..., c_k \right]^T.
\tag{23}
$$

The natural frequencies and corresponding mode shapes can be obtained by solving equation (22).

3. Numerical Results and Discussion

In this section, the calculation results are compared with those in the existing literature, and their convergence is studied to verify the accuracy of the established model. Then, the free vibration traveling wave behavior of the VTRCS is analyzed through parameter research. Unless otherwise

mentioned, the length of the VTRCS $L = 1$ m, the initial thickness $h_0 = 0.02$ m, the thickness variation parameter $k_h = 0.5$, the density $\rho = 1072$ kg/m^3, the elastic modulus $E = 172$ GPa, the shear modulus $G = 4.2$ GPa, and the Poisson's ratio $v = 0.31$, the average radius $R = 0.2$, the speed $\omega = 25$ r/s, the dimensionless frequency parameter $w^* = wR\sqrt{\rho/E}$, and the dimensionless speed $\Omega^* = \Omega R\sqrt{\rho/E}$.

3.1. Comparison and Convergence Research. Two cases are studied in this section to verify the accuracy and convergence of the proposed method.

3.1.1. Case One. The dimensionless frequency parameters (DFPs) of the backward wave and the forward wave for the RCS with uniform thickness under fixed (C-C) boundary conditions at both ends are given, respectively, and compared with the results in literature [27]. Also, the convergence research is conducted, and the calculation results under different number of truncation terms are listed, as shown in Tables 2 and 3. In this example, the aspect ratio of the RCS $L/R = 10$, the thick-aspect ratio $h/R = 0.05$, the Poisson's ratio $v = 0.3$, the dimensionless frequency parameter $w^* = wR\sqrt{\rho(1 - \mu^2)/E}$, and the dimensionless speed $\Omega^* = \Omega R\sqrt{\rho(1 - \mu^2)/E}$.

It can be seen from Tables 2 and 3 that the results are basically consistent with the results in literature [27]. The study shows that the calculation results converge to a certain value with the increase of the number of truncated terms $n$max, which have converged to a sufficiently accurate value when the number of truncated terms is 11, so $n$max is 11 in the following calculation.

3.1.2. Case Two. The second case gives the natural frequency (Hz) of the RCS with uniform thickness under simply supported (S-S) boundary conditions at both ends as shown in Table 4, which is compared with the results in literature [28]. The cylindrical shell length $L = 0.256$ m, average radius $R = 0.16$ m, thickness $h = 0.0025$ m, elastic modulus $E = 110$ GPa, Poisson's ratio $v = 0.31$, density $\rho = 4480$ kg/m^3, axial half wave number $m = 1$, and rotational speed $\Omega = 20000$ r/min.

It is observed in Table 4 that the results obtained by the proposed model are basically consistent with those in literature [28], and the maximum error is less than 1%.

In short, the above two examples verify the correctness and convergence of the proposed method.

3.2. Parameter Study. The effects of different thickness variations, rotational speed, thickness variation parameters, aspect ratio, and thickness-to-diameter ratio on the traveling wave behavior of free vibration are discussed in order to obtain the vibration characteristics of the VTRCS under different thickness variations, as shown in Figures 3–7.

The variation of the DFPs w_b^* and w_f^* with the circumferential wave number n of the VTRCS is shown in Figure 3. In the figure, $V0$: $k_h = 0$, that is, the thickness of the

RCS is uniform and remains unchanged in the x-axis direction.

Figure 3 shows that the DFPs w_b^* and w_f^* for the RCS under thickness change rise with the increase of the wave number n in the boundary conditions of the S-S or C-C. The DFPs of the VTRCS are the maximum under $V0$ thickness changes form, and it is the minimum under $V1$ thickness changes form. The DFPs of the VTRCS under $V2$ thickness variation form are higher than those under the other two thickness variations when V0 thickness variation form is not considered, which are close to those under $V0$ thickness variation form. It is also obvious from Figure 3 that the DFPs of the VTRCS under the four thickness changes firstly disperse from the same initial value and then converge to the same value with the increase of circumferential wave number n.

The variation of the DFPs w_b^* and w_f^* with the thickness parameter k_h for the RCS under the three thickness forms when the rotational speed is, respectively, 0 r/s, 25 r/s, and 50 r/s, is shown in Figure 4.

It is seen from Figure 4 that the DFPs for the VTRCS decrease gradually with the increase of k_h under different rotational speed and thickness, and it is minimum in the condition of the $V2$ thickness change. In addition, it can also be found that the rotational speed has almost no influence on the variation trend of the k_h.

The variation of the DFP w^* as the changing of Ω is shown in Figure 5 to further study the influence of rotational speed on the traveling wave for the VTRCS. The BW represents the backward wave, and FW represents the forward wave.

Figure 5 shows that the DFPs of backward wave rise with the increase of the rotational speed for the VTRCS, and the DFPs of forward wave reduce gradually with the increase of rotational speed. The DFP value of backward wave and forward wave under different rotational speed is the biggest under $V0$ thickness change form. The DFP value increases, and their difference becomes smaller under $V2$ thickness variation form when the boundary conditions change from S-S to C-C. In addition, it can also be found that the difference between the DFPs under different thicknesses becomes significantly larger when the circumferential wave number changes from 1 to 2.

Finally, the influence of geometric parameters on the DFPs of VTRCS is studied in Figures 6 and 7. Figure 6 gives the variation of the DFP for the VTRCS with the changing of the aspect ratio L/R, and Figure 7 shows the changing of the aspect ratio R/h_0.

Figure 6 manifests that the DFPs of VTRCS decrease gradually with the increase of length-to-diameter ratio L/R. Particularly, the DFPs decrease rapidly when the length-to-diameter ratio is less than 3, and it decreases slowly when the length-to-diameter ratio is more than 3. It can be seen from Figure 7 that the backward wave w_b^* and the forward wave w_f^* both decrease first and then increase with the increase of the thickness-to-diameter ratio for the DFP for the VTRCS. It can also be found from Figure 7 that the difference between the DFPs under the four thickness variation forms becomes smaller as the boundary conditions change from S-

TABLE 2: DFP of backward wave w_b^* for the RCS.

Ω^*	n	Saito and Endo [27]	Present					
			$n$max = 8	$n$max = 9	$n$max = 10	$n$max = 11	$n$max = 12	$n$max = 13
0.0025	2	0.05993	0.05989	0.05987	0.05987	0.05986	0.05986	0.05986
	3	0.11455	0.11462	0.11461	0.11461	0.11461	0.114641	0.11461
	4	0.21313	0.21317	0.21317	0.21317	0.21316	0.21316	0.21316
	5	0.34225	0.34226	0.34226	0.34226	0.34225	0.34225	0.34225
0.0050	2	0.06216	0.06212	0.06210	0.06210	0.06209	0.06209	0.06209
	3	0.11652	0.11660	0.11659	0.11659	0.11659	0.11659	0.11659
	4	0.21486	0.21490	0.21490	0.21490	0.21490	0.21490	0.21490
	5	0.34380	0.34381	0.34381	0.34381	0.34381	0.34381	0.34381

TABLE 3: DFP of forward wave w_f^* for the RCS.

Ω^*	n	Saito and Endo [27]	Present					
			$n$max = 8	$n$max = 9	$n$max = 10	$n$max = 11	$n$max = 12	$n$max = 13
0.0025	2	0.05593	0.05589	0.05587	0.05587	0.05586	0.05586	0.05586
	3	0.11155	0.11160	0.11160	0.11160	0.11159	0.11159	0.11159
	4	0.21078	0.21080	0.21080	0.21080	0.21080	0.21080	0.21080
	5	0.34033	0.34032	0.34031	0.34031	0.34031	0.34031	0.34031
0.0050	2	0.05460	0.05413	0.05410	0.05410	0.05409	0.05409	0.05409
	3	0.11058	0.11057	0.11057	0.11057	0.11056	0.11056	0.11056
	4	0.21018	0.21017	0.21016	0.21016	0.21016	0.21016	0.21016
	5	0.33997	0.33993	0.33993	0.33993	0.33992	0.33992	0.33992

Note. $n$max is the number of truncation terms and b and f represent the backward and forward waves, respectively.

TABLE 4: Comparisons of natural frequencies for the RCS.

Modes	f_b			f_f		
	FEM [28]	Present	Error (%)	FEM [22]	Present	Error (%)
(1, 3)	1830.45	1831.08	0.03	1436.24	1437.09	0.06
(1, 4)	1714.57	1713.40	0.07	1396.32	1395.50	0.06

Note. f_b and f_f represent the backward wave frequency and forward wave frequency, respectively.
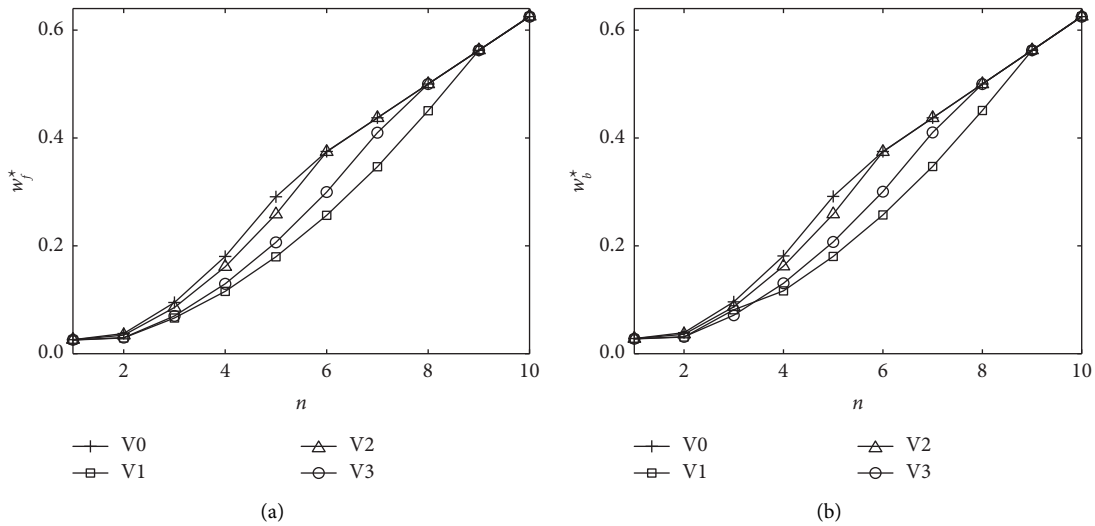
FIGURE 3: Continued.

(c)

(d)
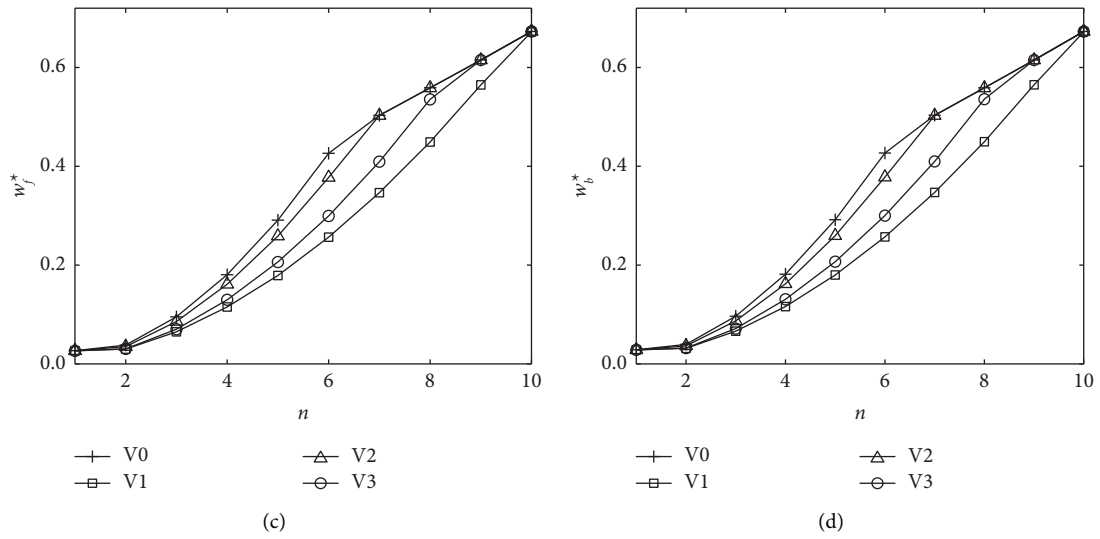
FIGURE 3: Variation of the DFP for the VTRCS with the circumferential wave number n. (a) S-S. (b) S-S. (c) C-C. (d) C-C.

(a)

(b)

(c)

(d)
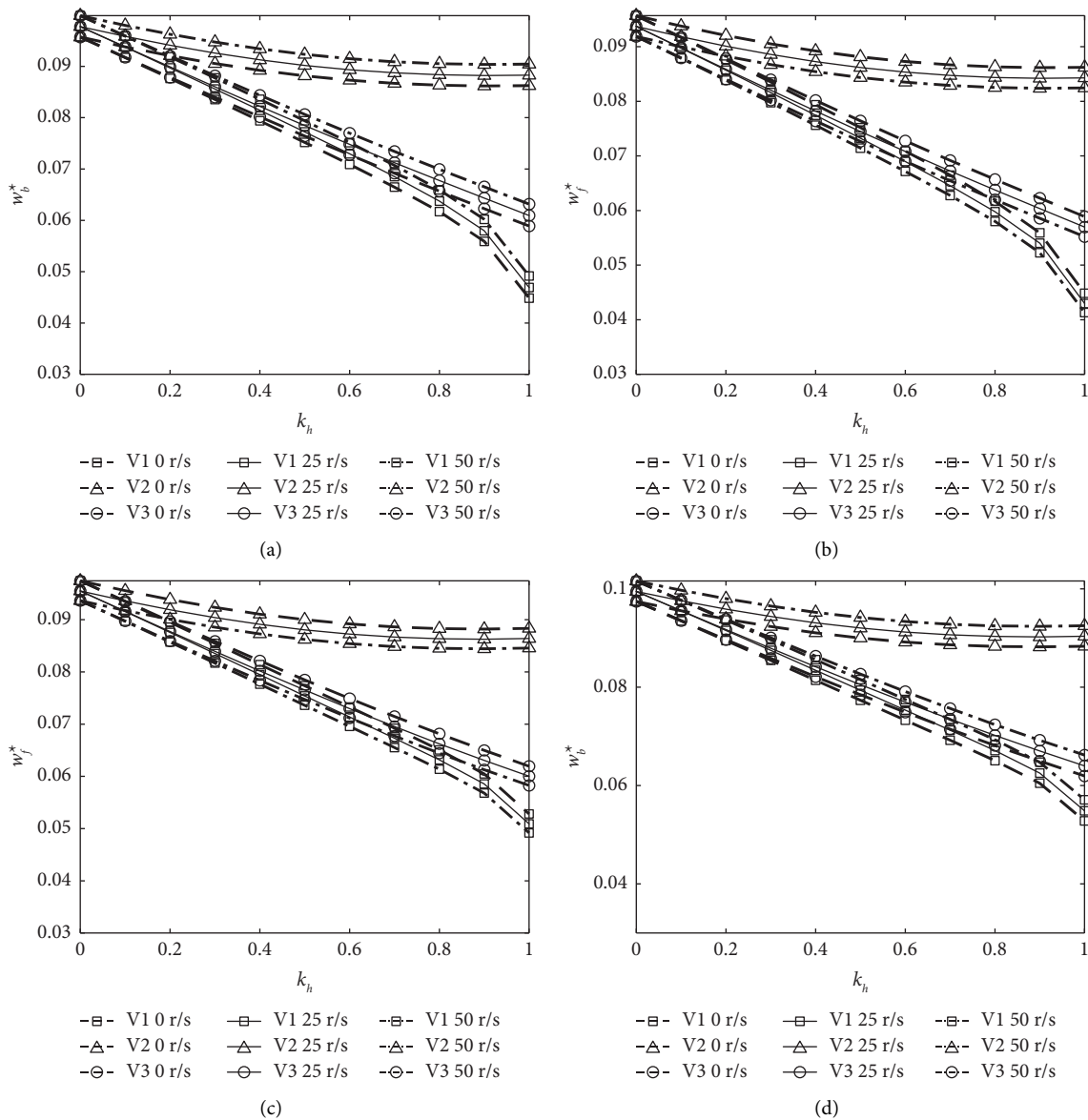
FIGURE 4: Variation of DFP for the VTRCS with k_h. (a) S-S. (b) S-S. (c) C-C. (d) C-C.

(a)

(b)

(c)

(d)
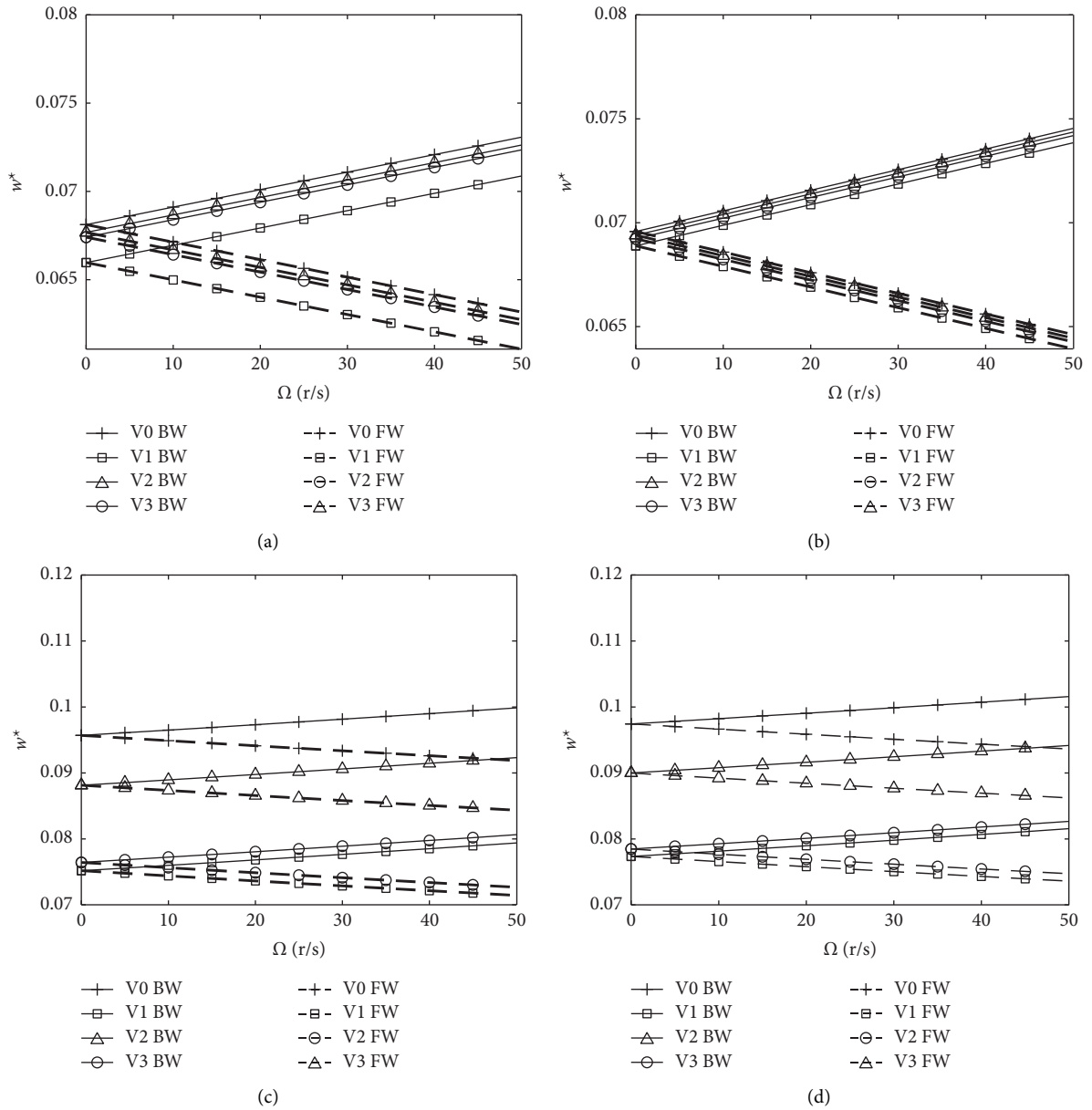
FIGURE 5: Variation of the DFP w^* for the VTRCS with the changing of Ω ($k_h = 0.5$). (a) S-S ($n = 1$). (b) C-C ($n = 1$). (c) S-S ($n = 2$). (d) C-C ($n = 2$).

(a)

(b)

(c)

(d)
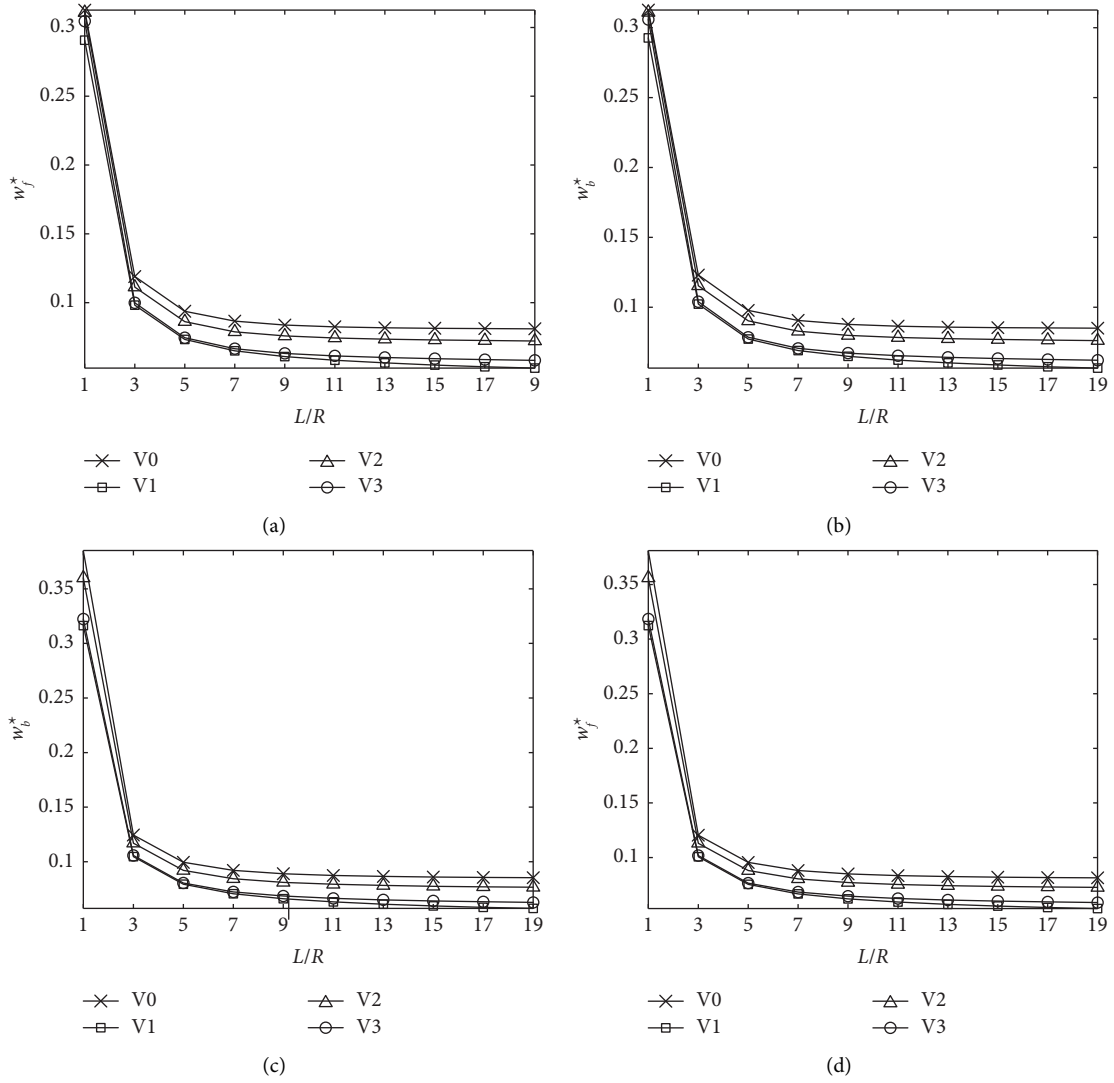
Figure 6: Variation of the DFP for the VTRCS with length to radius ratio L/R. (a) S-S. (b) S-S. (c) C-C. (d) C-C.

(a)

(b)
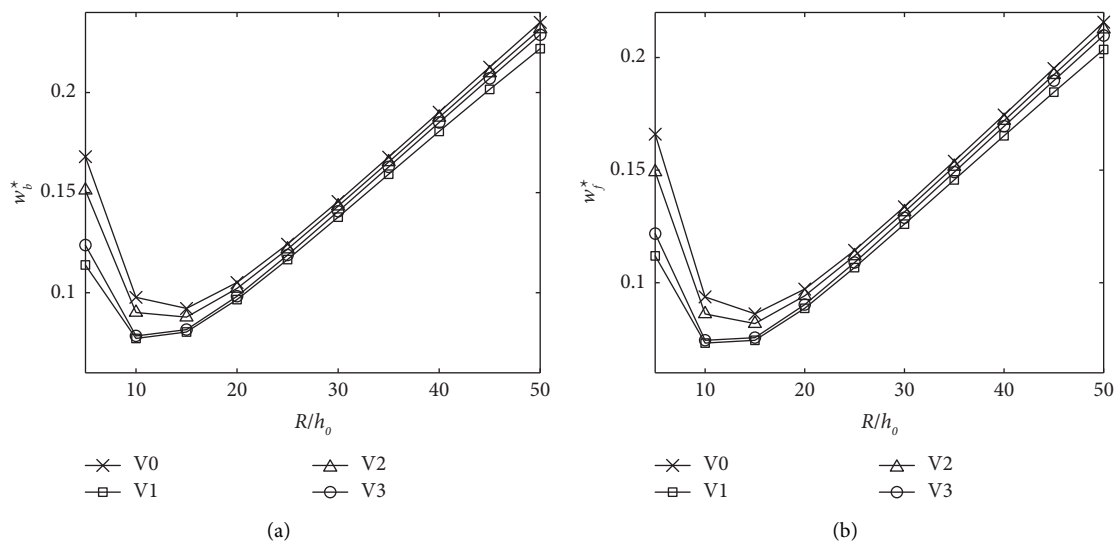
Figure 7: Continued.
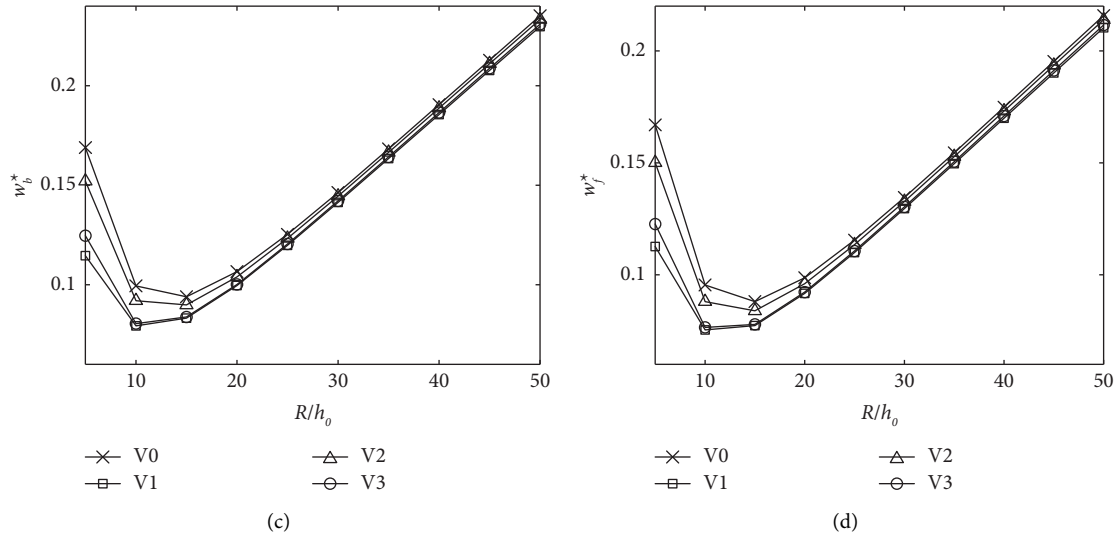
FIGURE 7: Variation of the DFP for the VTRCS with radius to thickness ratio R/h_0. (a) S-S. (b) S-S. (c) C-C. (d) C-C.

S to C-C. Specifically, the influence of thickness variation forms on the DFPs is little when the thickness-to-diameter ratio is higher than 25.

4. Conclusion

(1) The vibration characteristics of the VTRCS are investigated based on the Sanders shell theory via the Chebyshev–Ritz method. The correctness and convergence of the modeling method are verified through comparison and convergence research, and it is proved that the proposed model can effectively predict the traveling wave behavior of the free vibration for the VTRCS.

(2) The traveling wave DFP of the VTRCS rises with the increase of the wave number n under three thickness variation forms. The traveling wave DFP is the largest under $V0$, and it is higher than the other two kinds of thickness under $V2$ when $V0$ is not considered, which is close to the DFP in the $V0$. In addition, the DFP of the VTRCS first discretizes from the same initial value and then converges to the same value with the increase of circumferential wave number n under the four thickness variations.

(3) The traveling wave DFP of the VTRCS gradually decreases with the increase of the thickness change parameter kh at different speeds and different thicknesses. Among them, the traveling wave DFP change is the smallest under $V2$ and is significantly smaller than that of the other two thickness changes. The rotational speed has little effect on the variation trend of traveling wave frequency with thickness.

(4) The traveling wave DFP of VTRCS decreases gradually with the increase of aspect ratio L/R and decreases first and then increases with the increase of aspect ratio h_0/R. The difference between the DFPs becomes smaller under the four thickness variations as the boundary conditions change from S-S to C-C.

The variation of thickness has little effect on the traveling wave frequency when the thickness-to-diameter ratio is higher than a certain value.

Data Availability

The data used to support the findings of this study are currently under embargo while the research findings are commercialized. Requests for data, [6/12 months] after publication of this article, will be considered by the corresponding author.

Conflicts of Interest

The authors declare that there are no conflicts of interest regarding the publication of this article.

Acknowledgments

References

[1] X. Li, Y. Li, and T. Xie, "Vibration characteristics of a rotating composite laminated cylindrical shell in subsonic air flow and hygrothermal environment," *International Journal of Mechanical Sciences*, vol. 150, pp. 356–368, 2019.

[2] S. Sahmani and B. Safaei, "Large-amplitude oscillations of composite conical nanoshells with in-plane heterogeneity including surface stress effect," *Applied Mathematical Modelling*, vol. 89, pp. 1792–1813, 2021.

[3] M. Talebitooti, "Thermal effect on free vibration of ring-stiffened rotating functionally graded conical shell with clamped ends," *Mechanics of Advanced Materials and Structures*, vol. 25, no. 2, pp. 155–165, 2018.

[4] M. Hussain and M. N. Naeem, "Effects of ring supports on vibration of armchair and zigzag FGM rotating carbon nanotubes using Galerkin's method," *Composites Part B: Engineering*, vol. 163, pp. 548–561, 2019.

[5] Y. Heidari, M. Irani Rahaghi, and M. Arefi, "Free vibration analysis of a porous rotor integrated with regular patterns of circumferentially distributed functionally graded piezoelectric patches on inner and outer surfaces," *Journal of Intelligent Material Systems and Structures*, vol. 32, no. 1, pp. 82–103, 2021.

[6] H. SafarPour, K. Mohammadi, and M. Ghadiri, "Influence of various temperature distributions on critical speed and vibrational characteristics of rotating cylindrical microshells with modified length scale parameter," *The European Physical Journal Plus*, vol. 132, no. 6, pp. 1–19, 2017.

[7] H. SafarPour, B. Ghanbari, and M. Ghadiri, "Buckling and free vibration analysis of high speed rotating carbon nanotube reinforced cylindrical piezoelectric shell," *Applied Mathematical Modelling*, vol. 65, pp. 428–442, 2019.

[8] R. Rostami and M. Mohammadimehr, "Vibration control of rotating sandwich cylindrical shell-reinforced nanocomposite face sheet and porous core integrated with functionally graded magneto-electro-elastic layers," *Engineering with Computers*, vol. 38, pp. 87–100, 2020.

[9] A. Shokrgozar, H. Safarpour, and M. Habibi, "Influence of system parameters on buckling and frequency analysis of a spinning cantilever cylindrical 3D shell coupled with piezoelectric actuator," *Proceedings of the Institution of Mechanical Engineers- Part C: Journal of Mechanical Engineering Science*, vol. 234, no. 2, pp. 512–529, 2020.

[10] H. Amirabadi, F. Farhatnia, S. A. Eftekhari, and R. Hosseini-Ara, "Free vibration analysis of rotating functionally graded gpl-reinforced truncated thick conical shells under different boundary conditions," *Mechanics Based Design of Structures and Machines*, vol. 10, 2020.

[11] M. Mahinzare, H. Akhavan, and M. Ghadiri, "A nonlocal strain gradient theory for rotating thermo-mechanical characteristics on magnetically actuated viscoelastic functionally graded nanoshell," *Journal of Intelligent Material Systems and Structures*, vol. 31, no. 12, pp. 1511–1523, 2020.

[12] B. J. Yan, H. J. Liang, M. J. Jin, Z. L. Li, and Y. Song, "Vibration-damping characteristic analysis of constrained stand-off layer damping cylindrical shell using Rayleigh-Ritz method," *Engineering Computations*, vol. 37, no. 1, pp. 93–119, 2019.

[13] X. Y. Song, T. N. Cao, P. X. Gao, and Q. K. Han, "Vibration and damping analysis of cylindrical shell treated with viscoelastic damping materials under elastic boundary conditions via a unified Rayleigh-Ritz method," *International Journal of Mechanical Sciences*, vol. 165, Article ID 105158, 2020.

[14] V. L. Nguyen, M. T. Tran, S. Limkatanyu, and J. Rungamornrat, "Free vibration analysis of rotating fgp sandwich cylindrical shells with metal-foam core layer," *Mechanics of Advanced Materials and Structures*, vol. 10, 2022.

[15] F. Abbaspour and S. Hosseini, "Free vibration analysis of graphene platelets reinforced laminated piezoelectric cylindrical micro-shells using the Chebyshev-Ritz formulation," *Journal of Vibration Engineering & Technologies*, vol. 10, no. 6, pp. 2129–2141, 2022.

[16] Z. Y. Qin, Z. B. Yang, J. Zu, and F. L. Chu, "Free vibration analysis of rotating cylindrical shells coupled with moderately thick annular plates," *International Journal of Mechanical Sciences*, vol. 142-143, pp. 127–139, 2018.

[17] Z. Y. Qin, X. J. Pang, B. Safaei, and F. L. Chu, "Free vibration analysis of rotating functionally graded CNT reinforced composite cylindrical shells with arbitrary boundary conditions," *Composite Structures*, vol. 220, pp. 847–860, 2019.

[18] Z. Y. Qin, B. Safaei, X. J. Pang, and F. L. Chu, "Traveling wave analysis of rotating functionally graded graphene platelet reinforced nanocomposite cylindrical shells with general boundary conditions," *Results in Physics*, vol. 15, Article ID 102752, 2019.

[19] X. Song, J. Zhai, Y. Chen, and Q. Han, "Traveling wave analysis of rotating cross-ply laminated cylindrical shells with arbitrary boundaries conditions via Rayleigh–Ritz method," *Composite Structures*, vol. 133, pp. 1101–1115, 2015.

[20] H. Li, H. Y. Lv, T. A. Zhang et al., "Modeling and evaluation of dynamic degradation behaviours of carbon fibre-reinforced epoxy composite shells," *Applied Mathematical Modelling*, vol. 104, pp. 21–33, 2022.

[21] B. C. Dong, H. Li, X. P. Wang et al., "Nonlinear forced vibration of hybrid fiber/graphene nanoplatelets/polymer composite sandwich cylindrical shells with hexagon honeycomb core," *Nonlinear Dynamics*, vol. 110, no. 4, pp. 3303–3331, 2022.

[22] H. Li, D. M. Liu, B. C. Dong et al., "Investigation of vibration suppression performance of composite pyramidal truss sandwich cylindrical shell panels with damping coating," *Thin-Walled Structures*, vol. 181, Article ID 109980, 2022.

[23] H. Li, H. Y. Lv, J. F. Gu et al., "Nonlinear vibration characteristics of fibre reinforced composite cylindrical shells in thermal environment," *Mechanical Systems and Signal Processing*, vol. 156, Article ID 107665, 2021.

[24] H. Li, Z. H. Wang, H. Y. Lv et al., "Nonlinear vibration analysis of fiber reinforced composite cylindrical shells with partial constrained layer damping treatment," *Thin-Walled Structures*, vol. 157, Article ID 107000, 2020.

[25] T. H. Quoc, D. T. Huan, and H. T. Phuong, "Vibration characteristics of rotating functionally graded circular cylindrical shell with variable thickness under thermal environment," *International Journal of Pressure Vessels and Piping*, vol. 193, Article ID 104452, 2021.

[26] Z. Lei, L. Zhang, and K. Liew, "Vibration analysis of CNT-reinforced functionally graded rotating cylindrical panels using the element-free kp-Ritz method," *Composites Part B: Engineering*, vol. 77, pp. 291–303, 2015.

[27] T. Saito and M. Endo, "Vibration of finite length, rotating cylindrical shells," *Journal of Sound and Vibration*, vol. 107, no. 1, pp. 17–28, 1986.

[28] Z. Wu, G. Yao, and Y. Zhang, "Vibration analysis of a thin eccentric rotating circular cylindrical shell," *Proceedings of the Institution of Mechanical Engineers- Part C: Journal of Mechanical Engineering Science*, vol. 233, no. 5, pp. 1588–1600, 2019.